Advances in data reduction of high-pressure x-ray powder diffraction data from two-dimensional detectors: a case study of schafarzikite ($FeSb_2O_4$)

2006 J. Phys.: Condens. Matter 18 S1021

(http://iopscience.iop.org/0953-8984/18/25/S09)

INSTITUTE OF PHYSICS PUBLISHING JOURNAL OF PHYSICS: CONDENSED MATTER

J. Phys.: Condens. Matter **18** (2006) S1021–S1037 doi:10.1088/0953-8984/18/25/S09

Advances in data reduction of high-pressure x-ray powder diffraction data from two-dimensional detectors: a case study of schafarzikite ($FeSb_2O_4$)

B Hinrichsen[1], R E Dinnebier[1], P Rajiv[1], M Hanfland[2], A Grzechnik[3] and M Jansen[1]

[1] Max-Planck-Institute for Solid State Research, Heisenbergstrasse 1, D-70569 Stuttgart, Germany
[2] European Synchrotron Radiation Facility, 6 rue Jules Horowitz, BP220, 38043 Grenoble Cedex, France
[3] Departamento de Fisica de la Materia Condensada, Facultad de Ciencia y Technologia, Universidad del Pais Vasco, Apartado 644, E-48080 Bilbao, Spain

E-mail: r.dinnebier@fkf.mpg.de

Received 19 December 2005, in final form 9 February 2006
Published 8 June 2006
Online at stacks.iop.org/JPhysCM/18/S1021

Abstract

Methods have been developed to facilitate the data analysis of multiple two-dimensional powder diffraction images. These include, among others, automatic detection and calibration of Debye–Scherrer ellipses using pattern recognition techniques, and signal filtering employing established statistical procedures like fractile statistics.

All algorithms are implemented in the freely available program package Powder3D developed for the evaluation and graphical presentation of large powder diffraction data sets.

As a case study, we report the pressure dependence of the crystal structure of iron antimony oxide $FeSb_2O_4$ ($p \leqslant 21$ GPa, $T = 298$ K) using high-resolution angle dispersive x-ray powder diffraction. $FeSb_2O_4$ shows two phase transitions in the measured pressure range. The crystal structures of all modifications consist of frameworks of $Fe^{2+}O_6$ octahedra and irregular $Sb^{3+}O_4$ polyhedra. At ambient conditions, $FeSb_2O_4$ crystallizes in space group $P4_2/mbc$ (phase I). Between $p = 3.2$ GPa and 4.1 GPa it exhibits a displacive second order phase transition to a structure of space group $P2_1/c$ (phase II, $a = 5.7792(4)$ Å, $b = 8.3134(9)$ Å, $c = 8.4545(11)$ Å, $\beta = 91.879(10)°$, at $p = 4.2$ GPa). A second phase transition occurs between $p = 6.4$ GPa and 7.4 GPa to a structure of space group $P4_2/m$ (phase III, $a = 7.8498(4)$ Å, $c = 5.7452(5)$ Å, at $p = 10.5$ GPa). A nonlinear compression behaviour over the entire pressure range is observed, which can be described by three Vinet equations in the ranges from $p = 0.52$ GPa to $p = 3.12$ GPa, $p = 4.2$ GPa to $p = 6.3$ GPa and from $p = 7.5$ GPa to $p = 19.8$ GPa. The extrapolated bulk moduli of the high-pressure phases were determined to $K_0 = 49(2)$ GPa for phase I, $K_0 = 27(3)$ GPa for phase II and $K_0 = 45(2)$ GPa for phase III. The

crystal structures of all phases are refined against x-ray powder data measured at several pressures between $p = 0.52$ GPa, and 10.5 GPa.

(Some figures in this article are in colour only in the electronic version)

M Supplementary data files are available from stacks.iop.org/JPhysCM/18/S1021

1. Introduction

With the general availability of high-intensity parallel synchrotron radiation, the use of two-dimensional detectors like CCD-detectors or online image plate readers for fast high-resolution data acquisition is enjoying a growing popularity. As a consequence, the field of x-ray powder diffraction has experienced a renaissance. For the first time it is now possible to record the entire Debye–Scherrer rings up to high angular range with high angular resolution within a few seconds or even less. The field of applications is vast, with current experiments including texture analysis (Wenk and Grigull 2003) and the dependence of *in situ* powder diffraction measurements on pressure (Hanfland *et al* 1999), temperature (Norby 1997), chemical composition (Meneghini *et al* 2001), electric and magnetic fields (Knapp *et al* 2004) or external strains (Poulsen *et al* 2005).

The experimentalist is faced with two major challenges. First, large area detectors produce large numbers of two-dimensional images which need to be reproducibly reduced to one-dimensional powder patterns. Second, the sets of hundreds or even thousands of powder patterns need to be evaluated and presented graphically.

It is interesting to note that for both tasks only very few generally available programs exist. These are keyed toward single powder patterns involving extensive manual interaction. This approach is unsuitable for mass data analysis: not only is the manual workload exorbitant but the induced subjectivity hinders reproducible results.

The key to solving the first problem lies in the reliable extraction of a powder diffraction pattern unaffected by grain size effects, detector aberrations, and scattering from other sources like reaction cells, diamond anvils, gaskets, etc. Almost all signals from a two-dimensional image can be reduced to simple geometric figures like points, lines and ellipses, calling for the application of modern pattern recognition techniques (Fisker *et al* 1998, Theodoridis and Koutroumbas 1999, Paulus and Hornegger 1995). As to the representation and evaluation of the integrated powder patterns, a high-level graphically powerful programming language offers the basis for an efficient solution. We decided on the Interactive Data Language IDL (RSI 2005 current version 6.2) to develop a general program for automatic data reduction and evaluation of two-dimensional powder diffraction data called Powder3D. Some of the aspects necessary to solve the problems encountered during the investigation of the crystal structure of $FeSb_2O_4$ at high pressure are described in this paper.

$FeSb_2O_4$, also known as the mineral schafarzikite (Krenner 1921), belongs to a group of compounds crystallizing in space group $P4_2/mbc$ with the general formula AB_2O_4: A = Pb, Cu, Sn, Ni, Zn, Mn, Fe; B = Pb, As, Sb, where B represents ions with a stereochemically active lone electron pair. Generally they are regarded as pseudo-ligands that are able to replace one or more of the regular ligands in a given coordination sphere leading to irregular polyhedra of a low coordination number. The resulting stereochemical implications have been discussed in depth (Gillespie 1967a, 1967b, Gillespie and Robinson 1996a, 1996b).

The crystal structure of schafarzikite is characterized by the presence of edge-sharing iron octahedra connected with corner-sharing antimony tetrahedra leading to open channels

Table 1. Structural parameters of the ambient and low pressure structure of Schafarzikite which crystallizes in the space group $P4_2/mbc$. The parameters were refined to data collected at $p = 0.5$ GPa ($a = 8.5758(1)$ Å, $c = 5.8983(1)$ Å).

Atom:Wyck.	Fe:4d	Sb:8h	O:8g	O:8h
x/a	0	0.175(1)	0.676(1)	0.099(1)
y/b	1/2	0.164(1)	1.176(1)	0.651(1)
z/c	1/4	0	1/4	0

containing the lone pairs (Fischer and Pertlik 1975). The open channel structure (see table 1 for the ambient and low pressure structural parameters) and the high polarizability of the cations exhibiting the 'lone-pair' make it highly susceptible to pressure induced phase transitions. A previous high-pressure investigation of the related compound $Pb^{4+}Pb_2^{2+}O_4$ (Dinnebier *et al* 2003) showed two phase transitions towards two phases of higher density at pressures of $p = 0.11$–0.3 GPa and $p = 5.54$–6.6 GPa respectively, where the lone pair of the latter phase almost vanished tending towards an s-state character. While minium also shows several phase transitions upon cooling (Gavarri *et al* 1978), no phase transitions of schafarzikite on cooling to $T = 2$ K have been observed (Gonzalo *et al* 1966, Chater *et al* 1985). In this work, we have investigated the pressure dependence of the crystal structure of schafarzikite up to a pressure of $p = 19.8$ GPa. For this purpose, *in situ* x-ray powder diffraction measurements were performed at room temperature and elevated pressures using a diamond-anvil cell (DAC).

2. Experimental details

2.1. Synthesis and x-ray diffraction measurements

$FeSb_2O_4$ was prepared according to procedures described in the literature (Chater *et al* 1985).

For the x-ray powder diffraction experiments, a hand-ground sample of schafarzikite was loaded in a membrane driven diamond-anvil cell (DAC) (Letoullec *et al* 1988), using nitrogen (cryogenic loading) as pressure medium. The DAC had 300 μm culet and 125 μm hole diameters. The pressure was determined by the ruby luminescence method using the wavelength shift calibration of Mao *et al* (1986). High-pressure x-ray powder diffraction data were collected at room temperature at beamline ID9 of the European Synchrotron Radiation Facility (ESRF) using an experimental configuration following that described by Schulze *et al* (1998). Monochromatic radiation for the high-pressure experiment was selected at 30.0 keV (0.413 25 Å). The beam-size was 30 μm × 30 μm. Diffracted intensities were recorded with a Marresearch Mar345 online image plate system. A set of 22 images at selected pressures between $p = 0.56$ GPa and $p = 19.8$ GPa was recorded. Three of the 22 images were taken during the decompression of the sample. An exposure time of 120 s was chosen.

2.2. Data reduction and filtering

Information required for powder diffraction analysis is contained in Debye–Scherrer cones. These are projected as ellipses onto two-dimensional detectors (He 2003). A precise calibration of the experiment necessitates the exact definition of these cones. Currently, solving this task is a rather cumbersome ordeal. We have thus developed a robust method for the automatic detection and characterization of ellipses using a modified Hough transformation (Hough 1962). The method involves no mathematical complexity and exhibits excellent overall efficiency.

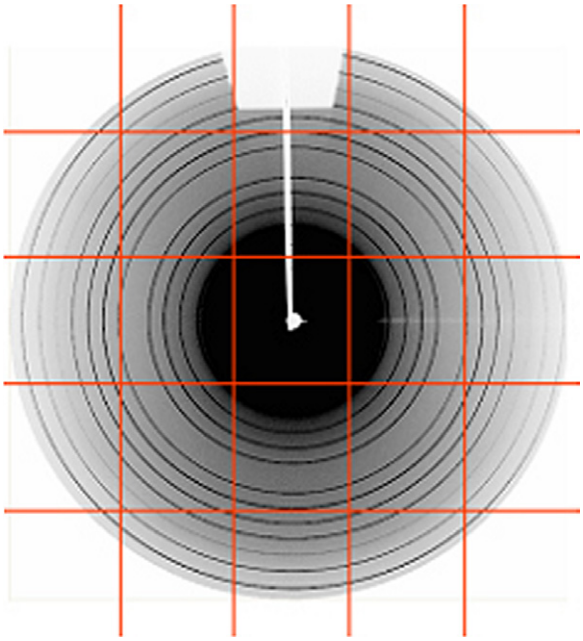

Figure 1. Centre detection grid.

2.3. Ellipse detection

An ellipse can be described by five parameters, the major axis a, minor axis b, centre coordinates x_0 and y_0 and angle of orientation α. Computing all five parameters simultaneously using Hough transformation is computationally very expensive (Bennett *et al* 1999), as a huge quantized five-dimensional parameter space has to created. In practice the transformation scales to the number of dimensions in parameter space. In order to reduce the size of the required parameter space, the complete process of ellipse detection is decomposed into different steps. Hough transformation is used for the calculation of the parameter b alone. Hence we require only a one-dimensional parameter space.

2.4. Reduction of resolution

The spatial resolution of digitized powder diffraction images is typically in the order of a few thousand pixels squared. Manipulation of such an amount of data is impractical. The computational complexity of an image of size $N \times N$ is $(N \times N)^4$. To improve the execution speed the image resolution is reduced by a factor of five.

2.5. Approximate centre determination

Many methods have been used for the determination of the centre of an ellipse (Lei and Wong 1999, Dammer *et al* 1997). Most of the methods suffer either a lack of accuracy or inefficient memory usage. We propose a generic two-step approach to determine the centre coordinates of an ellipse. In the first step we find the approximate centre by using the intensity patterns of vertical and horizontal grids (figure 1) drawn on the image.

All pixel intensities along a grid are copied to an array (figure 2). The mirror plane of this distribution is detected by finding the absolute difference of the mirrored intensities. This

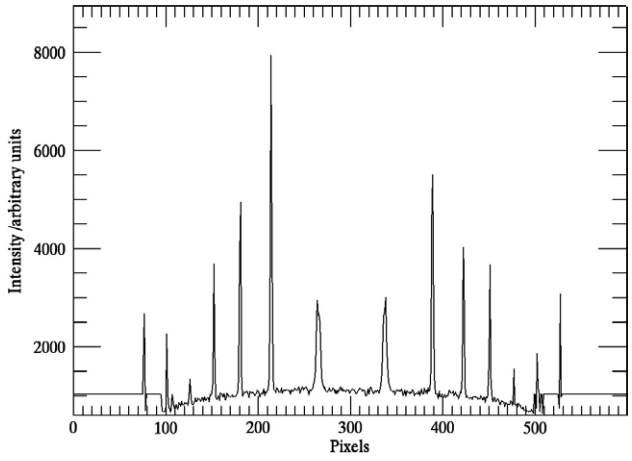

Figure 2. Profile along a grid line.

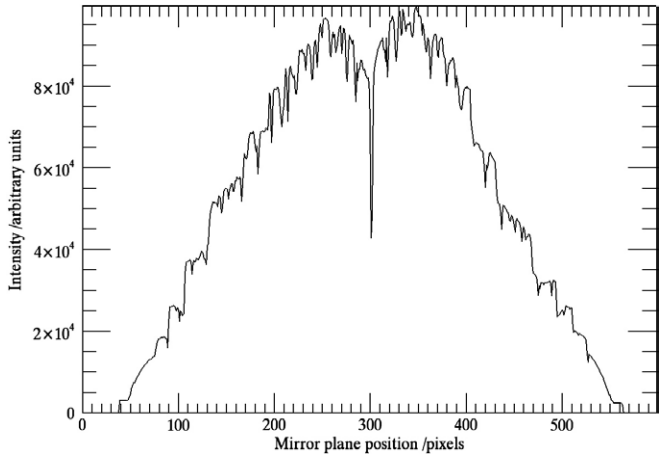

Figure 3. Difference histogram of profile.

absolute difference is calculated for each possible mirror plane position and copied to another array (figure 3). The lowest point in this difference plot is the position of maximum peak overlap and represents the approximate mirror plane. Each grid line results in one such point.

Two lines, one for the points from the vertical grids and the other from the horizontal grid, are fitted, using the robust least absolute deviation (Press *et al* 2002) method. The approximate centre of the ellipse is the point of intersection. This algorithm for centre determination is both robust against the outliers in the image and against the position of the ellipses with respect to the image centre. This method requires the centre of the ellipses to be on the image.

2.6. Masking of high-intensity spikes

High-intensity pixels have to be masked to enhance the accuracy of the ellipse parameter determination. Masking is done by capping the intensities to six times the median of the entire image.

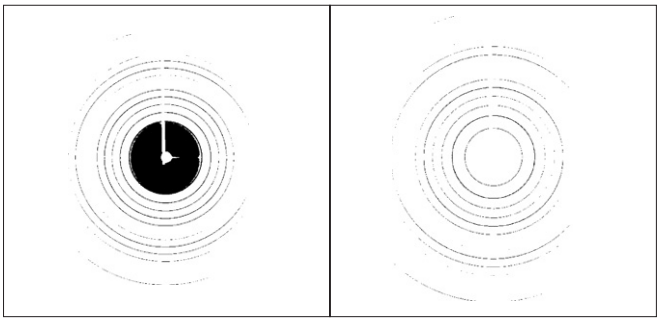

Figure 4. Binary images without (left) and with (right) initial background subtraction.

2.7. Background reduction and thresholding

Thresholding is an important step in preparing an image for a Hough transformation and the importance of a preceding background reduction will be shown. Diffraction images often suffer from a diffuse background resulting from the scattering of x-rays by air molecules. Hence the background intensity is high near the incident beam and decreases towards higher 2Θ angles. Subtracting the background for such images with nonuniform intensity distribution is crucial.

The entire image is divided into broad circular segments whose average intensities decrease toward higher radii. Background reduction is accomplished by subtracting twice the median of the pixel intensities within a segment from those same pixel intensities.

Following the background subtraction, the image is converted into a binary image. This conversion is beneficial to an efficient Hough transformation, as the number of transformed pixels is reduced and the space required for their storage is substantially smaller (Fung *et al* 1996). We set the pixels of high intensity to 1 and the remaining to 0 by applying a threshold of 10% of the maximum intensity. The result and the importance of an initial background reduction is visible in figure 4. In the further process of ellipse detection, only pixels with the value of 1 are subject to analysis.

2.8. Range of the major and minor axes

To restrict the search area for the major and minor axes of the ellipse we find the approximate range of a. The range of a and b is determined for each ellipse by calculating the radial distances. This is done only for a thin wedge of the image. For better averaging, 16 wedges are drawn with an opening angle of 2.5°. An opening angle of 2.5° seemed a good compromise between a local probe and a statistically acceptable sample.

After computing 16 radii of all the ellipses, the entire array of distances is converted into a histogram, containing the density of distances falling within certain intervals (figure 5). An algorithm that scans through the histogram identifies the ranges of the filled bins. These ranges, which correspond to the minimum and maximum distances to the centre, are initial estimates of the minor and major axes.

2.9. Determination of major axis and orientation

A routine based on Chellali and Fremont (2003) is used for the final steps. We assume a pair of pixels to be the vertices of the major axis of the ellipse. Their distance to one another is calculated, and should it lie within the range estimated previously, the midpoint is calculated.

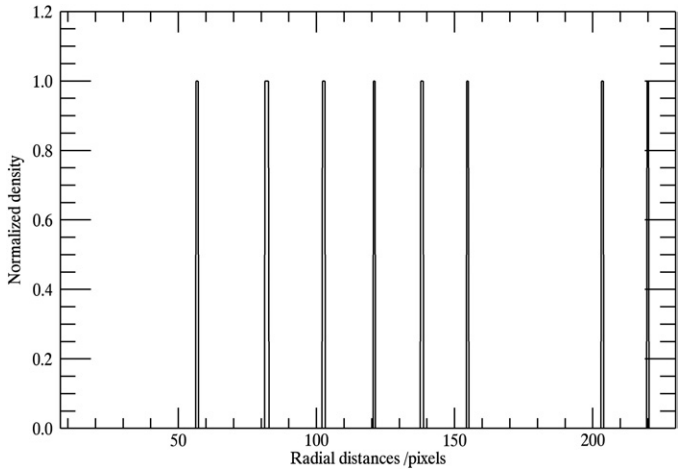

Figure 5. Radial distances of ellipses.

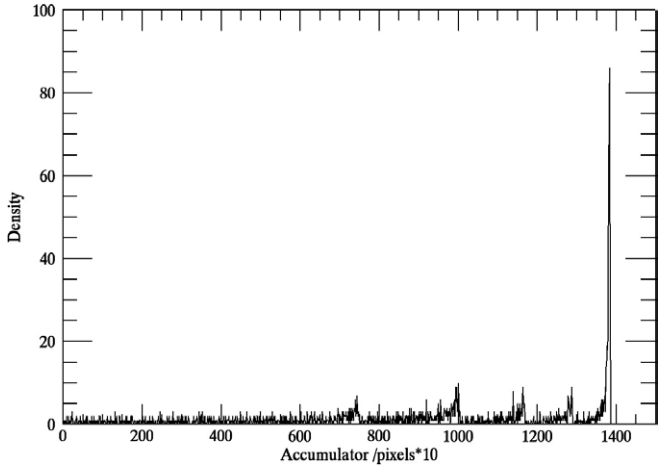

Figure 6. The accumulator array.

Should this again agree within a certain tolerance to the initial centre, then it is stored. The corresponding orientation of the ellipse is then calculated. Finally the maximum distance is taken to be the most probable value of the major axis of the ellipse. The average of all stored orientations is saved as the orientation estimate.

2.10. Determination of minor axis using Hough transformation

Hough transformation is a standard tool in image analysis and is widely applied to detect geometrical shapes. This Hough space spans all possible parameters that could describe the required shape. It is clear that the size of this space depends strongly on the number of parameters, which translate to Hough space dimensions, as well as the range of these parameters, which correspond to the lengths of the dimensions. The transformation is implemented by quantizing the Hough space into finite intervals. After processing all the pixels of the reduced image, the local peaks in the parameter space correspond (figure 6) to

the parameters of the most successful shapes. We have reduced the size of the transformation from five dimensions down to one by previously locating estimates for the centre, major axis and rotation angle. All pixels are checked for validity with regard to these estimates and the parameter space is incremented for all the pixels satisfying the constraints. After processing all the points in the image, the local maxima of the parameter space is the minor axis length (figure 6). As we use the Hough transformation to determine the minor axis only, a mere one-dimensional parameter space is required. This is beneficial to both computing and memory costs.

In the process of ellipse detection we determine the parameters of the innermost ellipse first and then proceed outwards. The reason is that the x-ray diffraction intensities have high gradients with the maximum near the centre of diffraction pattern. Outer ellipses thus have a lower signal density than inner ellipses. This results in better statistics for inner ellipses. After detecting an ellipse, its pixels are removed from the image, and the rest of the ellipses are detected iteratively. As a result the computational time for b decreases with every detected ellipse.

2.11. Signal filtering

Many powder diffraction experiments impede the realization of ideal circumstances, namely the contribution of a very large number of evenly sized and randomly oriented crystals to the diffraction pattern. This would in turn lead to an ideal normal intensity distribution. Despite the great experimental effort expended to ensure good quality data, high-pressure powder diffraction traditionally suffers from weaker signal quality than other *in situ* experiments. Sample rotation is confined to small angular rocking due to the DAC's opening angle, the wish to limit the effect of gasket shadowing and the avoidance of diamond reflections. This can lead to an extremely 'spotty' diffraction cone, the result of relatively few crystallites passing through a diffraction position, an effect that is enhanced by highly parallel synchrotron beams. To remedy this effect the intensity of the entire diffraction cone is integrated to a peak. This method generally results in powder patterns with reliable intensities.

One effect that is however not alleviated by a mere integration is that of highly dispersed intensities within the diffraction cone. These result from large grain size differences within the sample. Strong peaks resulting from larger grains lie within a ring of moderate intensities generated by small crystallites (figure 7). In most cases the number of large grains tends to be a couple of orders of magnitude lower than the number of small grains. On account of the small number of large crystallites they inevitably fail to ensure a 'statistical' distribution. Due to their high intensity, they have a great effect on the integrated pattern, falsifying the intensities considerably. All attempts to fit a pseudo-Voigt function to the peaks produced by an unfiltered integration failed. It should be mentioned that pseudo-single-crystal data can be extracted from such high intensity peaks (Schmidt *et al* 2003), this promising method lies outside the scope of the work presented here.

The accepted manner of filtering such data is to mask the high-intensity peaks manually using software such as Fit2D (Hammersley *et al* 1996). Manual masking is however time consuming, lacks reproducibility and relies too heavily on visual inspection to produce reliable results. Two exceptions known to the authors are Two2One (Vogel *et al* 2002) which is a filter based on Poisson statistics, and Datasqueeze (Heiney 2005) which contains an averaging filter aimed at removing bad pixels. These methods failed on our samples as our experimental distributions deviate strongly from the well known statistical models. For the analysis of our data we devised a two-dimensional signal filtering algorithm which should be generally applicable.

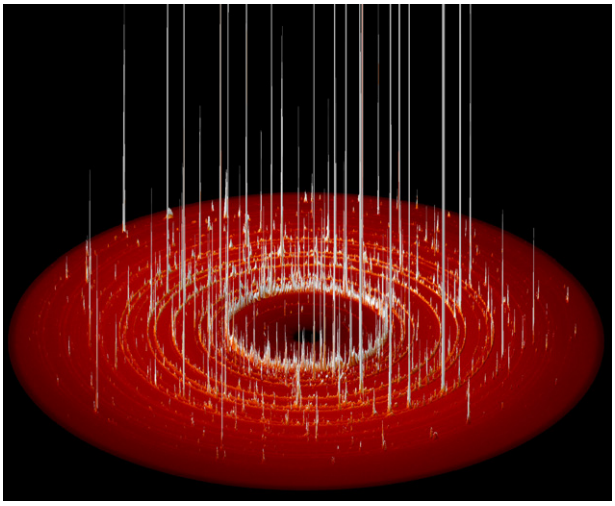

Figure 7. Rendered image plate data using a false colour texture map. Intensity is represented by the elevation along the z-axis. In addition the false colours have been scaled to the intensity. The scale has been adjusted to highlight the weak intensities.

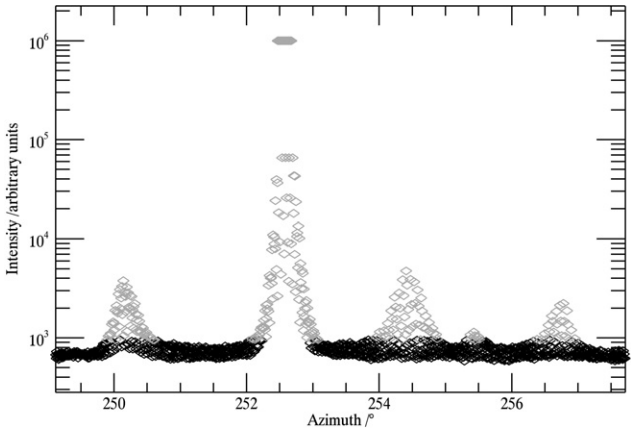

Figure 8. An excerpt of the azimuthal intensity distribution of the (004) reflection of $FeSb_2O_4$ at $p = 0.56$ GPa. Red diamonds represent data masked using the fractile threshold of 5%.

2.12. Fractile masking

The general goal of signal filtering is the separation of the required signal from artefacts or noise. We implement a robust type of band pass filter based on fractile statistics. Unlike model based filters, the fractile method is insensitive to strong statistical aberrations and was successfully applied to our data. An arbitrary fraction of the highest intensities collected for a 2Θ range is masked. In our case, by selecting 5% of the highest peaks, most of the pixels contributing to the high-intensity data are masked (figure 8). This selection was motivated by inspection of the integrated pattern. No further reduction in the integrated intensities could be observed using higher exclusion limits, thus the value of 5% was chosen. Mask dilation applied afterward suffices to mask the tails of the peaks (figure 9), leading to a significant improvement

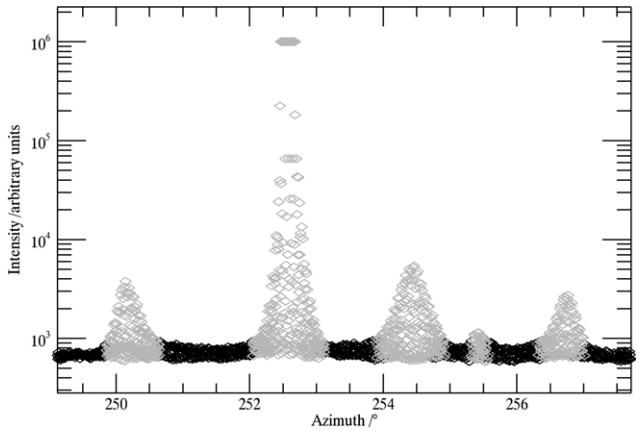

Figure 9. Same as figure 8. In addition the mask is dilated by two pixels.

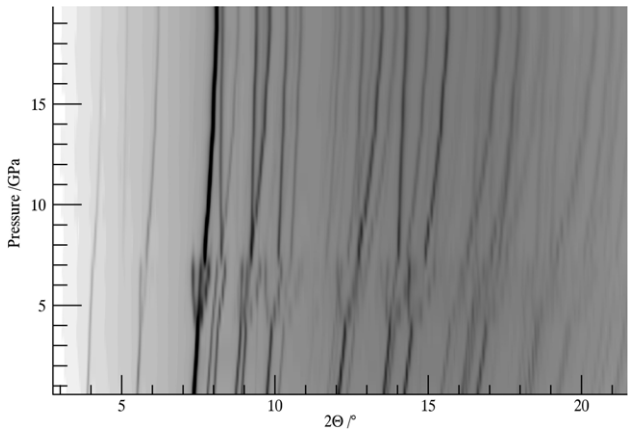

Figure 10. Simulated Guinier plot showing the progression of the powder pattern over the measured pressure range.

in intensity distribution of the signal. The diffraction intensities originating from the finely crystalline matrix are in effect the base line displayed as black diamonds in figures 8 and 9.

For the application of such intensity sensitive filtering procedures it is of ultimate importance to have previously applied all possible two-dimensional corrections affecting the intensity. Of greatest importance are those corrections which are a function of the azimuth. These include polarization and Lorentz corrections, for which the experimental geometry has to be determined. As the filter is applied sequentially to a small 2Θ range, the effect of corrections which are only a function of 2Θ have little impact. It should be further noted that for a correct error estimation (Chall *et al* 2000) a precise intensity distribution is essential. This can only be achieved by prior two-dimensional corrections.

2.13. Crystal structure determination and refinement

Following the successful filtering and integration of the two-dimensional images to conventional powder diffraction patterns, the dependence of the scattering profile of $FeSb_2O_4$ on the pressure (figure 10) gives evidence for a second order phase transition followed by a

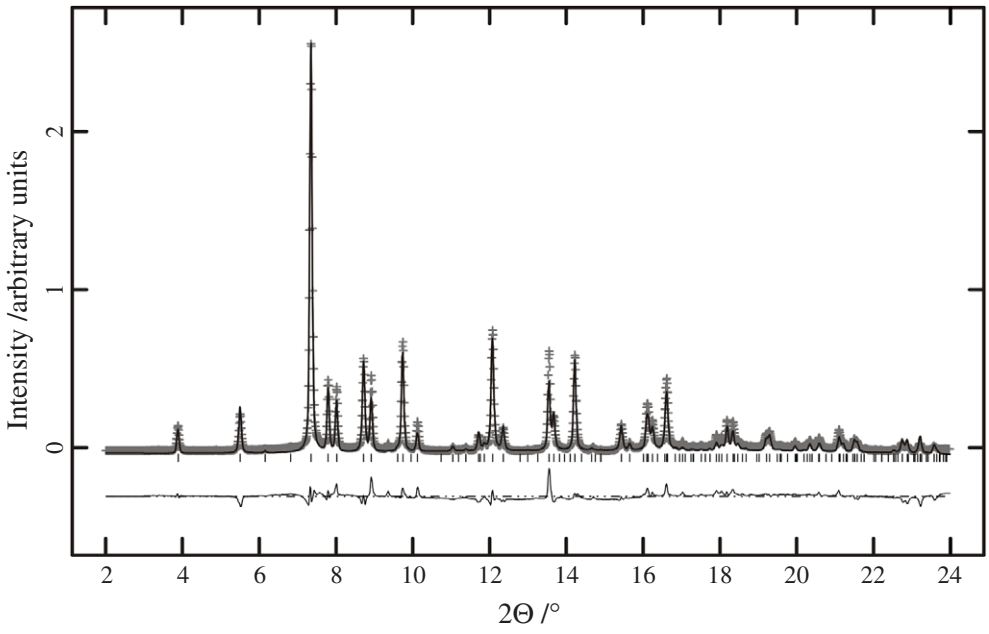

Figure 11. Scattered x-ray intensity for the low-pressure phase of $FeSb_2O_4$ at $p = 0.52$ GPa as a function of diffraction angle 2Θ. Shown are the observed pattern (crosses), the best Rietveld fit (thick black line), the difference curve (thin black line) and the reflection markers (vertical bars). The wavelength was 0.413 25 Å.

first order phase transition. The phase with tetragonal symmetry ($P4_2/mbc$) (phase I) which is stable at ambient conditions is retained up to at least $p = 2.2$ GPa. A transition into a phase with monoclinic symmetry ($P2_1/c$) (phase II) is observed to occur between $p = 2.2$ GPa and 3.1 GPa which is stable to at least $p = 8.3$ GPa. Between $p = 8.3$ GPa and $p = 9.5$ GPa a second phase transition occurs to another tetragonal phase ($P4_2/m$) (phase III) which stays stable until at least $p = 19.8$ GPa (figure 11). For all data sets, lattice parameters as a function of pressure were obtained by Le Bail type fits using the programmes FULLPROF (Rodríguez-Carvajal 2001) and GSAS (Larson and Von Dreele 1994), and are available as supplementary material (see stacks.iop.org/JPhysCM/18/S1021).

The background was modelled using the program Powder3D (figure 11) (Hinrichsen *et al* 2005). The peak-profile was described by a pseudo-Voigt function. The phenomenological microstrain model of Stephens (Stephens 1999) as implemented in GSAS was used to model the anisotropy of the FWHM. Four parameters were refined for the tetragonal phase. The quality of the powder patterns of all phases was sufficient to extract lattice parameters and to verify the crystal structures via Rietveld refinement (tables 1–4).

The powder patterns of phases II and III contained sufficiently resolved diffraction peaks to allow for *ab initio* crystal structure determination as well as for Rietveld refinement. The direct method program EXPO (Altomare *et al* 2005) was used to determine the positions of the iron and antimony atoms. Subsequent Rietveld refinements in combination with difference-Fourier analyses then revealed the positions of the oxygen atoms in the asymmetric unit. For the Rietveld refinements using the program GSAS, the lattice and reflection profile parameters were first kept at the values as obtained from the Le Bail fits. Slack soft constraints for the four Fe^{2+}–O bond lengths of 2.1(1) Å were used to stabilize the refinements. The atomic

Table 2. Details of the refinement phases I, II and III of $FeSb_2O_4$.

Pressure (GPa)	0.5	4.2	10.5
Space group	$P4_2/mbc$	$P2_1/c$	$P4_2/m$
ρ_{calc} (g cm^{-3})	5.564	5.945	6.818
Formula weight	363.37	363.37	363.37
Temperature (K)	290	290	290
R_p (%)[a]	2.0	1.7	1.9
R_{wp} (%)[a]	2.8	2.5	3.1
R_{exp} (%)[a]	5.6	5.7	5.8
R_{F^2} (%)[a]	29.9	14.7	17.4
No. of reflections	133	187	212
No. of variables	21	43	30
No. of refined atoms	4	7	6
Wavelength (Å)	0.413 251	0.413 251	0.413 251
2Θ range (deg), counting time	2.0–24.46, 120	2.0–24.46, 120	2.0–24.46, 120
Step size (deg 2Θ) (after rebinning)	0.01	0.01	0.01

[a] $R_p = \sum |I_O - I_C| / \sum I_O$, $R_{wp} = \sqrt{\sum w(I_O - I_C)^2 / \sum w I_O^2}$, $R_{exp} = \sqrt{(n-p)/\sum w I_O^2}$, $R_{F^2} = \sum |F_O^2 - F_C^2| / \sum F_O^2$ where I_O = observed intensity, I_C = calculated intensity, F_O = observed structure factor, F_C = calculated structure factor, w = weighting per data point, n = number of data points, p = number of parameters.

Table 3. The Vinet equation of state for the three phases of $FeSb_2O_4$ and related compounds.

Vinet EoS	V_0 (Å^3)	K_0 (GPa)	K_0'	R_w (%)
$FeSb_2O_4$ (phase I)	438(1)	49(2)	4 (fix)	2.21
$FeSb_2O_4$ (phase II)	459(6)	27(3)	4 (fix)	1.12
$FeSb_2O_4$ (phase III)	425(2)	45(2)	4 (fix)	2.28
$FeSb_2O_4$		50[a]		
Pb_3O_4 (phase II)	511(1)	20.8(4)[b]	4 (fix)	3.65
Pb_3O_4 (phase III)	222(2)	98(3)[b]	4 (fix)	4.25
Pb_3O_4		67(16)[c]		
$SnSb_2O_4$		49(8)[c]		
$NiSb_2O_4$		57[a], 65(5)[d]		
$ZnSb_2O_4$		52(9)[c]		
$MnSb_2O_4$		55[a]		

[a] Gavarri and Chater (1989) (calculated values).
[b] Dinnebier *et al* (2003).
[c] Gavarri (1982) (calculated values).
[d] Chater *et al* (1987) (measured at $T = 63$ and 240 K).

displacement parameters for the oxygen had to be restrained to be equal in the monoclinic phase, to hinder some parameters having physically meaningless negative values. For the same reason one oxygen atom in the low pressure phase and all oxygen atoms in the high pressure phase had to be refined with fixed isotropic atomic displacement parameters.

2.14. Equation of state

Lattice parameters as a function of pressure were extracted from each diffraction pattern. The derived volume/pressure dependence is represented by the equation of state (EoS). An EoS is typically fitted to a model based either on series expansion of Eulerian strain (Birch–Murnaghan EoS, Murnaghan 1944) or on cohesive energies in a condensed system (Vinet EoS, Vinet *et al*

Table 4. Wyckoff splitting for the phase transitions $P4_2/mbc \rightarrow P2_1/c \rightarrow P4_2/m$.

Atom:Wyck.	Fe:4d	Sb:8h		O:8g		O:8h	
Site symm.	..2	m..		2.22		m..	
x/a	0	0.175(1)		0.676(1)		0.099(1)	
y/b	1/2	0.164(1)		1.176(1)		0.651(1)	
z/c	1/4	0		1/4		0	
u_i (Å^2)	0.018(1)	0.004(2)		0.096(11)		0.001	
	↓	↓	↓	↓	↓	↓	↓
Atom:Wyck.	Fe:4e	Sb:4e	Sb:4e	O:4e	O:4e	O:4e	O:4e
Site symm.	1	1	1	1	1	1	1
x/a	0.224(3)	−0.010(2)	0.498(2)	0.223(6)	0.269(6)	0.017(6)	0.500(4)
y/b	0.0000(2)	0.172(2)	0.842(2)	0.697(5)	0.333(5)	0.094(2)	0.352(4)
z/c	0.496(3)	0.158(2)	0.181(2)	0.163(4)	0.804(5)	0.680(3)	0.088(2)
u_i (Å^2)	0.003(5)	0.022(6)	0.050(4)	0.06(1)	0.06(1)	0.06(1)	0.06(1)
	↓	↓	↓	↓	↓	↓	↓
Atom:Wyck.	Fe:4i	Sb:4j	Sb:4j	O:8k		O:4j	O:4j
Site symm.	2..	m..	m..	m..		m..	1
x/a	0	−0.164(2)	0.328(2)	0.681(5)		0.113(8)	0.483(8)
y/b	1/2	0.154(3)	0.653(3)	1.132(5)		0.636(9)	0.246(8)
z/c	0.222(5)	0	0	0.220(8)		0	0
u_i (Å^2)	0.007(6)	0.016(8)	0.028(5)	0.001		0.001	0.001

1986). The programme EOSFIT 5.2 (Angel 2002) was used to fit the Vinet EoS defined as

$$P = 3K_0 \frac{(1 - f_v)}{f_v^2} \exp\left(\frac{3}{2}\left(K_0' - 1\right)(1 - f_v)\right),$$

where

$$f_v = \left(\frac{V}{V_0}\right)^{1/3}$$

with volume at zero pressure V_0, the bulk modulus K_0, and its pressure derivative at zero pressure K_0'. In all calculations K_0' was selected as 4. The experimentally obtained values for the bulk modulus K_0 presented in table 3 show good agreement with calculated values for the low-pressure tetragonal phase I, being identical within experimental error. Higher compressibility expressed by the lower bulk modulus for the intermediate phase II of $FeSb_2O_4$ is a feature shared by the intermediate phase II of Pb_3O_4. The increase in compressibility of the monoclinic phase is roughly by a factor of two. No difference within experimental error is registered for the EoS between the low-pressure and high-pressure phases. It should be noted that the EoS of the first and second phases have been determined using only four and three data points respectively. Thus the interpretation of these values is somewhat speculative.

An anisotropy in the change of lattice parameters induced by pressure has also been observed in the high-pressure study of Pb_3O_4. The monoclinic phase II of $FeSb_2O_4$ shows a strong distortion of the lattice. The highest observed discontinuities of the lattice constants relate however to the re-entry of the tetragonal symmetry above $p = 7.4$ GPa (figures 12 and 13). A moderate compression of the c-axis until this pressure can be noted. For the remaining range up to $p = 19.8$ GPa the c-axis remains virtually unchanged. The entire compression in this range takes place within the ab-plane and is directly related to the constriction of the open channels containing the lone electron pairs.

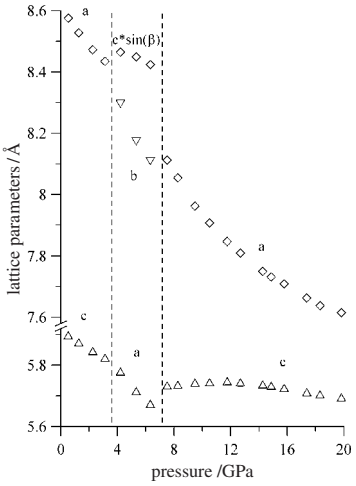

Figure 12. Dependence of the lattice parameters of $FeSb_2O_4$ on pressure in the range $p = 0$–19.8 GPa.

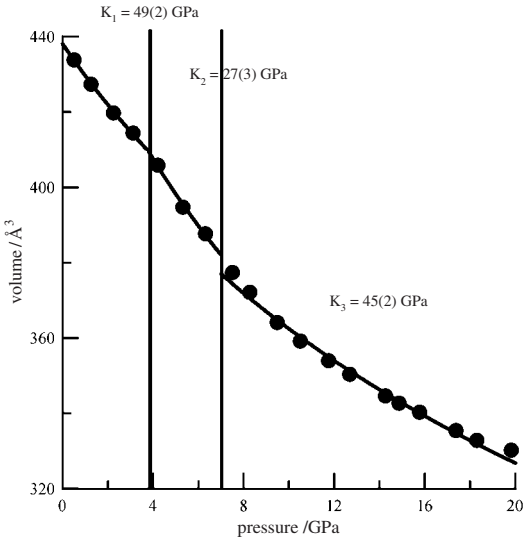

Figure 13. Dependence of the volume of $FeSb_2O_4$ on pressure in the range of $p = 0$–19.8 GPa. Smooth solid lines correspond to the least square fits of the Vinet equations of state.

2.15. Symmetry relations

Translationengleiche group–subgroup relations can be found for all phases. They are $P4_2/mbc \rightarrow t4 \rightarrow P2_1/c \rightarrow t8 \rightarrow P4_2/m$ and $P4_2/mbc \rightarrow t2 \rightarrow P4_2/m$. The initial path leads over $Pbam$, a space group type known from the high-pressure phase of Pb_3O_4 but not observed for $FeSb_2O_4$. Four possible paths lead back from $P2_1/c$ to $P4_2/m$ as can be seen in figure 14.

Symmetrical considerations would suggest the orthorhombic space group *Pbam* to bridge the higher and lower space groups (figure 14). The space group type *Pbam* is a known low-temperature/high-pressure space group type for minium (Pb_3O_4). A direct transition path

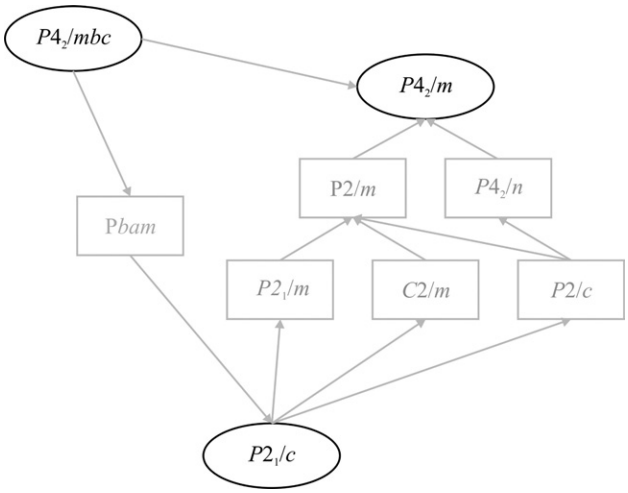

Figure 14. Group–subgroup tree of the observed phases. Grey lines are possible transition paths.

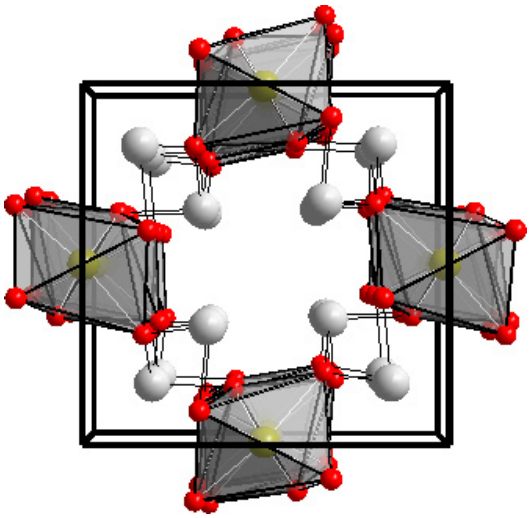

Figure 15. Low-pressure tetragonal $FeSb_2O_4$ (phase I) viewed down the *c*-axis, grey spheres within the polyhedra represent Fe, large light-grey spheres Sb.

from the ambient pressure space group $P4_2/mbc$ to the high-pressure space group $P4_2/m$ is symmetrically plausible as $P4_2/m$ is a non-isomorphic maximal subgroup of $P4_2/mbc$. The second transformation from $P2_1/c$ to $P4_2/m$ would require two further space groups (figure 14).

The structure of $FeSb_2O_4$ (figure 15) is dominated by infinite chains of edge-linked distorted $Fe^{2+}O_6$ octahedra. The chains project down the *c*-axis and lie centred on the *a*- and *b*-axes akin to the orientation of the TiO_6 octahedra in the rutile structure. All Sb^{3+} ions are located in the planes spanned by the shared edges of neighbouring octahedral chains. Their polyhedra link the $[FeO_6]^1_\infty$ chains. Sb is coordinated by three O atoms, two representing the apex of neighbouring FeO_6 octahedra from one chain and one equatorial oxygen from a neighbouring chain. This results in a slightly irregular SbO_3 pyramid with oxygen forming

the base and the lone pair electrons representing the apex. Four of these pairs point inward to the channel, resulting in a large unoccupied space. Thus the channels are lined by trigonal pyramids of SbO_3, the closest Sb–Sb distance being 3.53 Å.

In the monoclinic phase II all atoms are on the general 4e position (table 4). The special positions and the high tetragonal symmetry are recovered at higher pressures. The mechanism of the first phase transition can be interpreted as an initial continuous shearing toward the monoclinic symmetry. The shearing presents itself in the growing monoclinic angle, corresponding to the angle of the *c*-axis to the *ab*-plane in the tetragonal phases I and III. The distortion of the iron octahedra increases with pressure. All changes are however continuous, characteristic of a second order phase transition. The second transition is different. Sharp discontinuities of the lattice constants speak for a first order phase transition. The iron octahedra remain distorted; however, the orientation has changed substantially compared to that of phases I and II.

The change in the antimony environment is substantial for the second phase transition. Here one of the symmetry-independent antimony atoms takes on a fourfold coordination in contrast to the dominant threefold coordination for the remaining phases. It should be kept in mind that the refinement of the atomic position of weak x-ray scatterers such as oxygen in the vicinity of heavy atoms such as antimony, which are strong scatterers, is inherently difficult.

3. Conclusion

The general applicability of two-dimensional signal filtering to powder diffraction data has been demonstrated. In the presented case study of $FeSb_2O_4$, high-pressure data have been analysed, successfully identifying two new phases at non-ambient pressures. All applied filters have been implemented in the freely available software Powder3D.

References

Altomare A, Camalli M, Cuocci C, da Silva I, Giacovazzo C, Moliterni A G G and Rizzi R 2005 Space group determination: improvements in EXPO2004 *J. Appl. Crystallogr.* **38** 760–7

Angel R J 2002 *EOSFIT Version 5.2,* personal communication (available from http://www.crystal.vt.edu/crystal/software.html)

Bennett N, Burrigge R and Saito N 1999 A method to detect and characterize ellipses using Hough Transform *IEEE Trans. Pattern Anal. Mach. Intell.* **21** 7

Chall M, Knom K, Ehm L and Depmeier W 2000 Estimating intensity errors of powder diffraction data from area detectors *High Pressure Res.* **17** 315–23

Chater R, Gavarri J R and Hewat A W 1985 Structures isomorphes MeX_2O_4. Evolution structurale entre 2 K et 300 K de l'antimonite $FeSb_2O_4$: elasticite et ordre magnetique anisotropes *J. Solid State Chem.* **60** 78–86

Chater R, Gavarri J R and Hewat A W 1987 Évolution structurale sous pression de $NiSb_2O_4$: compressibilités anisotropes et ordre magnetique *J. Solid State Chem.* **67** 98–103

Chellali R and Fremont V 2003 Ellipse detection using Hough transform *13th Int. Conf. on Artificial Reality and Telexistence (Japan)*

Dammer C, Leleux P, Villers D and Dosiere M 1997 Use of Hough transform to determine the center of digitized x-ray diffraction patterns *Nucl. Instrum. Methods Phys. Res.* B **132** 214–20

Dinnebier R E, Carlson S, Hanfland M and Jansen M 2003 Bulk moduli and high pressure crystal structures of minium Pb_3O_4 determined by x-ray powder diffraction *Am. Mineral.* **88** 996–1002

Fischer R and Pertlik F 1975 Verfeinerung der Kristallstruktur des Schafarzikits, $FeSb_2O_4$ *Mineral. Petrol.* **22** 236–41

Fisker R, Poulsen H F, Schou J, Carstensen J M and Garbe S 1998 Use of image-processing tools for texture analysis of high-energy synchrotron data *J. Appl. Crystallogr.* **31** 647–53

Fung P F, Lee W S and King I 1996 Randomized generalized Hough transform for 2-D greyscale object detection *Proc. Int. Conf. on Pattern Recognition* vol 2, pp 511–5

Gavarri J R, Weigel D and Hewat A W 1978 Oxydes de plomb. IV. Evolution structurale de l'oxyde Pb_3O_4 entre 240 et 5 K et mecanisme de la transition *J. Solid State Chem.* **23** 327–39

Gavarri J R 1982 Evolution structurale de l'oxyde isomorphes MeX_2O_4: relation entre dilatation, vibrations et rigidite *J. Solid State Chem.* **43** 12–28
Gavarri J R and Chater R 1989 Structural evolution, magnetic transitions, and the Gruneisen constants of the antimonites $MeSb_2O_4$ *Phase Transit.* **14** 109–16
Gillespie R J 1967a Electron-pair repulsions and molecular shape *Angew. Chem.* **79** 885–96
Gillespie R J 1967b *Angew. Chem. Int. Edn Engl.* **6** 819–30
Gillespie R J and Robinson E A 1996a Electron-domains and the VSEPR model of molecular geometry *Angew. Chem.* **108** 539–60
Gillespie R J and Robinson E A 1996b *Angew. Chem. Int. Edn Engl.* **35** 495–514
Gonzalo J A, Cox D E and Shirane G 1966 The magnetic structure of $FeSb_2O_4$ *Phys. Rev.* **147** 415–8
Hammersley A P, Svensson S O, Hanfland M, Fitch A N and Hausermann D 1996 Two-dimensional detector software: from real detector to idealised image or two-theta scan *High Pressure Res.* **14** 235–48
Hanfland M, Schwarz U, Syassen K and Takemura K 1999 Crystal structure of the high-pressure phase silicon VI *Phys. Rev. Lett.* **82** 1197
He B 2003 Introduction to two-dimensional x-ray diffraction *Powder Diffract.* **18** 71–85
Heiney P A 2005 private communication
Hinrichsen B, Dinnebier R E and Jansen M 2006 Powder3D: An easy to use program for data reduction and graphical presentation of large numbers of powder diffraction patterns *Z. Kristallogr. Suppl.* **23** 231–6
Hough P V C 1962 Method and means for recognizing complex patterns *US Patent Specification* 3069654
Knapp M, Baehtz C, Ehrenberg H and Fuess H 2004 The synchrotron powder diffractometer at beamline B2 at HASYLAB/DESY: status and capabilities *J. Synchrotron Radiat.* **11** 328–34
Krenner J A 1921 Schafarzikit, ein neues Mineral *Z. Kristallogr.* **56** 198
Larson A C and Von Dreele R B 1994 GSAS—General structure analysis system *Los Alamos National Laboratory Report* LAUR 86-748
Lei Y and Wong K C 1999 Ellipse detection based on symmetry *Pattern Recog. Lett.* **20** 41–7
Letoullec R, Pinceaux J P and Loubeyre P 1988 *High Pressure Res.* **1** 77–90
Mao H K, Xu J and Bell P M 1986 Calibration of the ruby pressure gauge to 800 kbar under quasi-hydrostatic conditions *J. Geophys. Res.* **91(B5)** 4673–6
Meneghini C, Artioli G, Balerna A, Gualtieri A F, Norby P and Mobiliob S 2001 Multipurpose imaging-plate camera for *in situ* powder XRD at the GILDA beamline *J. Synchrotron Radiat.* **8** 1162–6
Murnaghan F D 1944 The compressibility of media under extreme pressure *Proc. Natl Acad. Sci.* **30** 244–7
Norby P 1997 Synchrotron powder diffraction using imaging plates: crystal structure determination and Rietveld refinement *J. Appl. Crystallogr.* **30** 21–30
Paulus D and Hornegger J 1995 *Pattern Recognition and Image Processing in C++* (Braunschweig: Vieweg)
Poulsen H F, Wert J A, Neuefeind J, Honkimäki V and Daymond M 2005 Measuring strain distributions in amorphous materials *Nat. Mater.* **4** 33–6
Press W H, Teukolsky S A, Vetterling W T and Flannery B P 2002 *Numerical Recipes in C* (Cambridge: Cambridge University Press)
Rodríguez-Carvajal J 2001 Recent developments of the program FULLPROF *Commission on Powder Diffraction Newsletter* **26** 12–9
RSI 2005 *Interactive Data Language—IDL* Boulder, CO, USA
Schmidt S, Poulsen H F and Vaughn G B M 2003 Structural refinements of the individual grains within polycrystals and powders *J. Appl. Crystallogr.* **36** 326–32
Schulze C, Lienert U, Hanfland M, Lorenzen M and Zontone F 1998 Microfocusing of hard x-rays with cylindrically bent crystal monochromators *J. Synchrotron Radiat.* **5** 77
Stephens P W 1999 Phenomenological model of anisotropic peak broadening in powder diffraction *J. Appl. Crystallogr.* **32** 281–9
Theodoridis S and Koutroumbas K 1999 *Pattern Recognition* (New York: Academic)
Vinet P, Ferrante J, Smith J R and Rose J H 1986 *J. Phys. C: Solid State Phys.* **19** 467–73
Vogel S, Ehm L, Knorr K and Braun G 2002 Automated processing of 2D powder data *Adv. X-ray Anal.* **45** 31
Wenk H R and Grigull S 2003 Synchrotron texture analysis with area detectors *J. Appl. Crystallogr.* **36** 1040–9